International Journal of Nanomedicine

Dovepress
open access to scientific and medical research

Open Access Full Text Article

ORIGINAL RESEARCH

Biocompatible Nanostructured Silver-Incorporated Implant Surfaces Show Effective Antibacterial, Osteogenic, and Anti-Inflammatory Effects in vitro and in Rat Model

Hui Gao[1,*], Nan Jiang[2,*], Qiannan Niu[3], Shenglin Mei[4,5], Håvard Jostein Haugen[6], Qianli Ma[6,7]

[1]Department of Stomatology, the Eighth Medical Center of Chinese PLA General Hospital, Beijing, People's Republic of China; [2]Department of Community Dentistry, Institute of Clinical Dentistry, University of Oslo, Oslo, Norway; [3]State Key Laboratory of Oral & Maxillofacial Reconstruction and Regeneration, National Clinical Research Center for Oral Diseases, Shaanxi Clinical Research Center for Oral Diseases, Department of Orthodontics, School of Stomatology, The Fourth Military Medical University, Xi'an, Shaanxi Province, People's Republic of China; [4]Xingrui Dental Clinic, Xi'an, Shaanxi Province, People's Republic of China; [5]Department of Physics & Materials Science, City University of Hong Kong, Hong Kong, People's Republic of China; [6]Department of Biomaterials, Institute of Clinical Dentistry, University of Oslo, Oslo, Norway; [7]Department of Immunology, School of Basic Medicine, Fourth Military Medical University, Xi'an, Shaanxi Province, People's Republic of China

*These authors contributed equally to this work

Correspondence: Håvard Jostein Haugen; Qianli Ma, Department of Biomaterials, Institute of Clinical Dentistry, University of Oslo, Oslo, 0317, Norway, Email h.j.haugen@odont.uio.no; qianlima@odont.uio.no

Introduction: Titanium (Ti) and its alloys are widely utilized in endosseous implants. However, their clinical efficacy is marred by complications arising from bacterial infections owing to their inadequate antibacterial properties. Consequently, enhancing the antibacterial attributes of implant surfaces stands as a pivotal objective in the realm of implantable materials research.

Methods: In this study, we employed sequential anodization and plasma immersion ion implantation (PIII) technology to fabricate a silver-embedded sparsely titania nanotube array (SNT) on the near-β titanium alloy Ti-5Zr-3Sn-5Mo-15Nb (TLM) implants. The surface characteristics, antimicrobial properties, biocompatibility, and osteogenic activity of the silver-nanomodified SNT implant (SNT Ag) surface, alongside peri-implant inflammatory responses, were meticulously assessed through a combination of in vitro and in vivo analyses.

Results: Compared with polished TLM and SNT, the silver-embedded SNT (SNT Ag) surface retained the basic shape of nanotubes and stably released Ag^+ at the ppm level for a long time, which demonstrated an effective inhibition and bactericidal activity against Staphylococcus aureus (SA) while maintaining ideal cytocompatibility. Additionally, the subtle modifications in nanotubular topography induced by silver implantation endowed SNT Ag with enhanced osteogenic activity and mitigated inflammatory capsulation in soft tissue peri-implants in a rat model.

Conclusion: Incorporating a silver-embedded SNT array onto the implant surface demonstrated robust antibacterial properties, impeccable cytocompatibility, exceptional osteogenic activity, and the potential to prevent inflammatory encapsulation around the implant site. The Silver-PIII modification strategy emerges as a highly promising approach for surface applications in endosseous implants and trans-gingival implant abutments.

Keywords: implant surface modification, silver PIII, anti-bacterial activity, cytocompatibility, osteogenic differentiation, host inflammatory response

Introduction

Titanium (Ti) and Ti alloys find extensive use in dental implants, orthopedic prostheses, artificial joints, and more, owing to their outstanding biocompatibility, osteointegration ability, corrosion resistance, and biomimetic mechanical-stress properties.[1,2] Despite their remarkable attributes, clinical applications of Ti implants face significant challenges, such as bacterial infections, impaired implant osseointegration, and inflammation-induced bone loss around implants.[3] The oral cavity and gingival cervical

Received: 15 August 2023
Accepted: 21 November 2023
Published: 6 December 2023

region surrounding implant abutments are teeming with bacteria, forming biofilms upon instant contact with implantable materials. These biofilms hinder the early attachment of host cells to the implant surface, triggering inflammation and detrimental immune responses in the surrounding soft tissue and bone, ultimately leading to implant failure.[4] Recent consensus reports identify bacterial biofilm as the primary cause of peri-implant mucositis and peri-implantitis, characterized by chronic inflammation, bone loss, and eventual loss of implant osteointegration.[5–7] Therefore, conferring Ti-based implant surfaces with desirable antibacterial activity is imperative to optimizing clinical outcomes and prognosis in implant therapy.[8]

Antibiotic and antimicrobial peptides (AMPs) have been functionalized as antibacterial agents on implant surfaces to prevent bacterial adhesion and biofilm formation.[9,10] However, their efficacy is hampered by challenges in release dynamics and concentrations, often leading to rapid release in the oral environment, short-term overdose, and difficulty maintaining long-term antibacterial properties.[11–15] Various biodegradable materials (eg, chitosan and phospholipid coating) were used to control the release of antibiotics and AMPs on Ti implants. Although the drug release slowed in the first few days, over 85% of antimicrobial agents were released between 7 and 15 days.[16,17] The rapid drug release and degradation of the surface coating may further alter the surface topography of the implant, thereby hindering the stability of the tissue-implant interface.[18] Moreover, the emergence of drug-resistant strains of bacteria poses a significant concern with antibiotic and AMP implant coatings.[19–21] In addition to the medicine-dependent strategy, surface charging also provided an excellent antibacterial property on the implant surface. Paul et al established a platform based on capacitive carbon-doped TiO_2 nanotubes. After positive direct current charging, such a platform exhibited ideal antibacterial performance induced by high discharging capacity.[22] The electro-antibacterial effects can be further promoted by mechanical intervention, which easily stiffens and rips the bacteria membrane, disturbing the electron balance and generating intracellular oxidative stress.[23]

In contrast to antibiotics and AMPs, inorganic silver (Ag) incorporation is considered an attractive antimicrobial agent due to its broad-spectrum activity against bacteria, fungi, and some virus species,[24–26] high stability in a physiological environment, and extremely low possibility of inducing drug-resistant strains.[27–29] Compared with the novel electro-mechanical antibacterial strategy, the Ag-incorporation strategy offers a long-term and stable antimicrobial surface on the implant, making it closer to clinical application and independent on technologically sensitive platforms, as reported previously.[23] However, with a narrow therapeutic window, Ag and Ag ions (Ag^+) may fail to exert their antimicrobial activity or exhibit toxicity at inappropriate concentrations.[30–32] Therefore, strict control over silver release by optimizing silver modification parameters on the implant surfaces is essential to achieving excellent antibacterial performance without compromising the original biological function of the host tissue.

An anodization-established biomimetic TiO_2 nanotube arrays (NTs) have been proven as biocompatible surface coatings on Ti implants.[33] Their unique nanotopography could enhance the osteogenic differentiation of human mesenchymal stem cells and regulate the innate inflammatory responses in peri-implant tissues.[33–36] The hollow structure of nanotubes was inferred to facilitate Ag reservation.[37] Our previous studies utilized plasma immersion ion implantation (PIII) technology to embed elemental Ag onto NT implant surfaces, exhibiting ideal antimicrobial effects. However, the implantation depth and morphology of the Ag layer were greatly subjected to the PIII voltage and nanotube distribution.[8] With excellent mechanical properties and a lower substrate elastic modulus (<70 GPa), the near-β titanium alloy Ti-5Zr-3Sn-5Mo-15Nb (TLM) is considered a promising implant material, demonstrating reduced modulus mismatch with natural bone.[38] In the present study, a sparsely distributed nanotube array (SNT) was fabricated on a TLM implant surface via anodization. Elemental Ag was uniformly incorporated into the SNT surface without compromising the basic TiO_2 nanotubular structure. This study aims to determine whether PIII Ag-incorporation technology imparts robust antibacterial properties and osteogenic activity on the SNT surface while minimizing adverse host inflammatory responses.

Materials and Methods

Sample Preparation and Characterization of Nanostructured TLM Samples with Ag PIII Treatment

The near β titanium alloy Ti-5Zr-3Sn-5Mo-15Nb (TLM) plate (1 mm in thickness) was donated by the Northwest Institute for Nonferrous Metal Research (Xi'an, People's Republic of China). It was cut into round disks with a diameter of 14 mm. The TLM disks were polished manually in one direction by SiC sandpaper (MATADOR, Germany) from 1500- to 5000-grit and

then subjected to ultrasonic cleaning in acetone, ethanol, and deionized water (dH_2O, Milli-Q water) each for 5 min in sequence. The polished TLM samples were set as controls. The vertically aligned sparsely nanotubular surfaces were fabricated using an anodization process as described previously.[33,39] In brief, with a graphite cathode, the TLM samples acted as an anode and were anodized in an F^--ion-containing electrolyte at 20 V for 1 h at 20°C using a DC power supply. The electrolyte consisted of 0.69 wt % hydrofluoric acid (Sigma–Aldrich, USA) and 6.9 wt % phosphoric acid in deionized water. The anodized TLM samples were denoted as SNT. Immediately after anodization, the samples were ultrasonically cleaned with deionized water and annealed at 450°C in dry air for 1 hour to transform the amorphous phase of the surface TiO_2 nanotubular layer into the anatase phase. Afterward, SNT samples were subjected to Ag plasma PIII as described previously.[8] Ag PIII was conducted using a filtered cathodic arc plasma source with a 99.99% pure Ag cathode. A curved magnetic duct was inserted between the plasma source and main chamber to remove macroparticles produced from the cathodic arc.[40] During Ag PIII, the pulse of the cathodic arc was synchronized with that of the target voltage. All the samples used for cell culture assays were sterilized by 75% ethanol orbital shaking for 1 hour, followed by ultraviolet A/C (UVA/C, λ = 365 nm(A)/254 nm(C), Philips, Poland) irradiation for 1 hour at a distance of 50 cm. The processing parameters of different samples are listed in Table 1.

Field emission scanning electron microscopy (FE-SEM, S-4800, Hitachi, Japan) and atomic force microscopy (AFM, NanoScope V MultiMode system, Veeco, USA) were employed to inspect the surface topography and roughness. The surface elemental composition and Ag distribution with depth were determined by X-ray photoelectron spectroscopy (XPS, PHI 5802, Physical Electronics, USA) equipped with a monochromatic Al K_α source and Ar ion etching unit. Constant pass energy (11.75 eV) was employed, and all the data were collected at a take-off angle of 45°. The etching parameter was set to 1.98 nm/0.5 min at 0–10 min, 3.97 nm/min at 10–30 min, and 7.94 nm/2 min afterward. The wettability of TLM samples was assessed by analyzing static liquid (deionized water, formamide, and diiodomethane, 10 μL/drop) contact angles by the DSA1 System (KRUSS, Germany). The surface energy (dispersed, polar, and total) was calculated by the Owens-Wendt-Rabel-Kaelble (OWRK) method as reported previously.[41,42] Six measurements were performed on each specimen for statistical accountability. The surface elastic modulus with depth was measured by a nanoIndenter (NMT-300, NANOVEA, USA).

The 30-day release of Ag from TLM samples (TLM, SNT, and SNT Ag) was inspected by inductively coupled plasma–mass spectrometry (ICP-MS, Thermo X series 2, USA). In brief, the TLM samples were immersed in 5 mL of phosphate-buffered saline (PBS, Gibco, Germany) at 37°C with orbital shaking at 60 rpm (to mimic physiological body fluid flow). After immersion for 1 h, 3 h, 12 h, 24 h, 3 days (d), 7 d, 15 d, 20 d, and 30 d the elutes were collected, and the cumulative Ag^+ release was analyzed (3 samples per group at each time point).

Antibacterial Activity of Nanostructured TLM Samples with Ag PIII Treatment

Staphylococcus aureus (SA, Cat No. 23235, ATCC, USA) was cultivated in 0.8% broth medium (Cat No. 234000, BD Biosciences, USA) under standard aerobic conditions (normal air, 37°C). The SA suspension was adjusted to a density of 1×10^6 CFU/mL and seeded on TLM samples (1 mL/sample) preplaced in 24-well plates.

1) Colony formation: After being cultured with SA for 3, 12 and 24 h, TLM samples were rinsed thrice with PBS to remove nonattached SA. The rinsed TLM samples were subjected to ultrasonication in 1 mL fresh PBS for 5 min to

Table 1 Parameters of Anodization and Ag PIII* for TLM, SNT and SNT Ag Samples Preparation

Sample Name	Anodization		Ag plasma Immersion Ion Implantation				
	Voltage (V)	Time (min)	Pressure (Pa)	Time (min)	Voltage (kV)	Pulse Frequency (Hz)	Pulse Duration (μs)
TLM	–	–	–	–	–	–	–
SNT	20	60	–	–	–	–	–
SNT Ag	20	60	1.8×10^{-4}	90	−1.5	10	3000

Note: *Plasma Immersion Ion Implantation.

obtain an SA suspension. The SA suspensions were diluted from 1 to 100 with PBS and were cultured on 2.3% agar plates (213000, BD Biosciences, USA) overnight for colony counting.

2) FE-SEM observation: After being cultured with SA for 3 and 24 h, TLM samples were rinsed thrice with warm PBS to remove nonattached SA and were fixed in 3% glutaraldehyde for 1 h at 4°C, followed by sequential ethanol dehydration (30, 50, 70, 90, and 100% ethanol) and drying (hexamethyldisilazane, 52619, Sigma–Aldrich, Germany). All TLM samples were sputter-coated with platinum before FE-SEM observation.

3) Laser scanning confocal microscopy (LSCM) analysis: After culture with SA for 3 and 24 h, TLM samples were rinsed three times with PBS and stained with a LIVE/DEAD™ BacLight™ Bacterial Viability Kit (L7012, Invitrogen, USA). SYTO9-labeled living SA and propidium iodide (PI)-labeled dead SA were captured by LSCM (FV1200, Olympus), and live/dead cell counting was conducted by ImageJ software (NIH, USA). The antibacterial activity of the TLM samples was divided into 2 parameters, growth inhibitory activity (GIA) and bactericidal activity (BA), which were calculated by the following formula: $\mathrm{GIA} = \frac{\mathrm{Count_{test.SYTO9}} - \mathrm{Count_{Ctr.STYO9}}}{\mathrm{Count_{Ctr.SYTO9}}} \times 100\%$

$Count_{test.\ SYTO9}$, counts of live SA on SNT or SNT Ag samples. $Count_{ctr.\ SYTO9}$, counts of live SA on TLM samples.

$$\text{the BA} = \frac{\mathrm{Count_{test.PI}} - \mathrm{Count_{Ctr.PI}}}{\mathrm{Count_{Ctr.PI}}} \times 100\%$$

$Count_{test.\ PI}$, counts of dead SA on SNT or SNT Ag samples. $Count_{ctr.\ PI}$, counts of dead SA on TLM samples.

The Cytocompatibility of Nanostructured TLM Samples with Ag PIII Treatment

The cytocompatibility evaluation was designed according to previous studies and ISO standards.[37,43,44] The aluminum ceramic disk was used as a negative control. In brief, the cytocompatibility evaluation was divided into two models (direct contact model and extract model) and two test assays (MTT and LDH assays).

1) For the MTT extract assay, TLM samples and negative controls (Al_2O_3 ceramic coins of the same size as TLM samples) were incubated in 5 mL of Eagle's minimum essential medium (EMEM, 30–2003, ATCC, USA) with 10% horse serum (26050088, Gibco, NZ) at 37°C for 1 day and 4°C for 30 d to obtain sample extracts. L929 cells (CCL-1, ATCC, USA) were seeded in 96-well plates (1000 cells/well) and cultured for 24 h. The culture media was discarded, and testing extracts and blank media were added to cells (100 μL/well) with a background control (only blank media without cells). After 24 h, the culture media were discarded, and 100 μL of 3-(4,5-dimethylthiazol-2-yl)-2,5-diphenyl tetrazolium bromide (MTT, M6494, Invitrogen, USA) media (1 mg/mL in EMEM) was added to each well. The cells were cultured for an additional 2 h to allow formazan formation. Then, MTT media were removed, and 50 μL of dimethyl sulfoxide (DMSO, Sigma) was added to each well to dissolve formazan. A microplate reader (ELX800, Biotek, USA) was used to read the optical absorbance at 540 nm. A decrease in cellular viability leads to a reduction in formazan formation and subsequent $\mathrm{absorbance_{540}}$. To measure the cytotoxicity of the tested extracts, the following equation was used:

$$\text{Relative cell viability}(\%) = \frac{\mathrm{Absorbance_{test}} - \mathrm{Absorbance_{background}}}{\mathrm{Absorbance_{blank}} - \mathrm{Absorbance_{background}}} \times 100\% \quad (1)$$

The tested sample was considered cytotoxic if the relative cell viability was <70%.

2) For the MTT direct contact assay, L929 cells were seeded on TLM and negative control samples at a density of 2×10^4 cells/sample and incubated for 1 and 3 d. After that, the culture media were discarded, and 1 mL MTT media were added to each well and cultured for 2 h. All the MTT media were removed, and 500 μL DMSO was added to each sample to dissolve the formazan. Then, 50 μL of DMSO was added to a new 96-well plate, and the absorbance was read at 540 nm. Equation (1) is used as described above to measure the cytotoxicity of the tested samples.

3) For the lactic dehydrogenase (LDH) extract assay, the preparation of sample extracts was the same as in the MTT assay. L929 cells were seeded in 96-well plates (1000 cells/well) and cultured for 24 h. The culture media were discarded, and testing extracts and blank medium were added to the cells (100 μL/well) with a background control (only blank medium without cells). After exposure to sample extracts for 24 h, all tested supernatants and corresponding toxicity positive controls (1% Triton X-100 added 1 h before sample collection, set as 100% cell damage) were collected and subjected to LDH assays (11644793001, Roche, USA) according to the manufacturer's instructions. The absorbance was read at 490 nm. The following equation calculated the relative cell damage:

$$\text{Relative cell damage} = \frac{\text{Absorbance}_{\text{test}} - \text{Absorbance}_{\text{blank}} - \text{Absorbance}_{\text{background}}}{\text{Absorbance}_{\text{positive}} - \text{Absorbance}_{\text{blank}} - \text{Absorbance}_{\text{background}}} \times 100\% \quad (2)$$

4) For the LDH direct contact assay, L929 cells were seeded on TLM and negative control disks (with background control) at a density of 2×10^4 cells/sample and incubated for 1 and 3 d. All tested supernatants and corresponding toxicity positive controls (1% Triton X-100 added 1 h before sample collection, set as 100% cell damage) were collected and subjected to the LDH assay. The relative cell damage is calculated by equation (2).

5) For FE-SEM observation: After being seeded with L-929 cells for 1 d, TLM samples were rinsed with PBS and fixed in 3% glutaraldehyde for 20 min at 4°C, followed by sequential ethanol dehydration and critical point drying. All TLM samples were sputter-coated with platinum before FE-SEM observation.

Osteogenic Activity of TLM Samples with Ag PIII Treatment

LSCM was employed to investigate the cell morphologic alteration on TLM samples. MG-63 human osteoblastic lineage cells (CRL-1427, ATCC, USA) were seeded on TLM samples at a density of 2×10^4 cells/mL/sample and cultured in growth medium (GM): EMEM with 10% fetal calf serum (10270–106, Gibco, Brazil) or osteogenic differentiation medium (OM): GM with 50 μg/mL ascorbic acid, 10 mM β-glycerophosphate (G9422, Sigma–Aldrich, USA) and 100 nM dexamethasone (D4902, Sigma–Aldrich, USA). After culturing for 1, 3, and 7 d, samples were fixed with 4% paraformaldehyde (PFA, 8187151000, Sigma–Aldrich, USA) for 20 min at room temperature (RT). After washing three times with cold PBS, the samples were blocked with 1% BSA/PBS buffer for 1 h at RT. Then, the samples were stained with Alexa Fluor™ 488 Phalloidin (A12379, Invitrogen, USA) and DRAQ5 (62251, Thermo Scientific, USA) and observed by LSCM under excitation/emission wavelengths of 495/518 nm and 647/>665 nm.

MG-63 cells were seeded on TLM samples and cultured in GM and OM as described above for 1, 3, and 7 d for proliferation viability assay. At the designated time points, the media were changed to 500 μL fresh CCK8 medium (GM or OM with 10% CCK-8, ab228554, Abcam, Netherlands), and the cells were cultured for an additional 2 h. The CCK8 medium was transferred to a new 96-well plate (100 μL/well), and the absorbance was read at 450 nm. The absorbance reflected the proliferation viability of MG-63 cells.

For the osteogenic gene expression profile of human osteoblasts, MG-63 cells were seeded on TLM samples at a density of 2×10^4 cells/mL/sample and cultured in OM for 3 and 7 d. Total mRNA from samples was isolated with an RNeasy Mini Kit (74104, Qiagen, Germany) and reverse transcribed to cDNA using a High-Capacity RNA-to-cDNA™ Kit (4388950, Applied Biosystems, Thermo Fisher Scientific, USA) according to the manufacturer's instructions. qPCR (CFX96TM PCR System, Bio-Rad, USA) was performed with a Human Osteogenesis TaqMan Gene Expression 96-well plate Array (4414227, Applied Biosystems, USA). The following data standardization and analysis were performed by RStudio (PBC, Boston, USA). The relative expression levels of SNT and SNT Ag were standardized by scale function and subjected to limma analysis to identify the differential expression profile, generate an expression heatmap, and conduct cluster analysis (ComplexHeatmap package) and principal component analysis (PCA) by the prcomp function in the stats package. In the follow-up analysis, the absolute value of logFC (log of fold change) greater than 1 was used as a filter condition to screen genes that may have differences in biological significance. The differentially expressed gene sets were mapped to the Gene Ontology database and subjected to biological process analysis entries (clusterProfiler package) that were significantly enriched by these genes.

ALP Production, Collagen Secretion and Extracellular Matrix (ECM) Mineralization on TLM Samples with Ag PIII Treatment

MG-63 cells were seeded on TLM samples at a density of 2×10^4 cells/mL/sample and cultured in OM for 7 (for ALP), 14 (for collagen) and 21 days (for ECM mineralization). 1) For ALP staining, samples were fixed in 4% paraformaldehyde for 20 min and incubated in NBT/BCIP solution (11697471001, Roche, USA) for 30 min, allowing the formation of dark-blue indigo precipitation on TLM samples. Images were captured by stereomicroscopy. 2) For collagen staining, samples were fixed in 4% paraformaldehyde for 20 min and stained in 0.1 wt% Sirius Red (365548, Sigma–Aldrich, USA) in saturated picric acid solution (P6744, Sigma–Aldrich, USA) for 20 h. The samples were washed with 0.1

M acetic acid (A6283, Sigma–Aldrich, USA) to remove excessive Sirius Red staining and then observed under a stereomicroscope. For semiquantitative analysis, each sample was eluted in 500 μL of elution solution (0.2 M NaOH/methanol 1:1, S5811 and 34860, Sigma–Aldrich, USA). The eluates were transferred to a new 96-well plate (100 μL/well), and the absorbance was then read at 562 nm. 3) For ECM mineralization, samples were fixed with 60% isopropanol (563935, Sigma–Aldrich, USA) for 1 min and then rehydrated in dH_2O for 3 min. The samples were stained with 40 mM alizarin red (ARS, pH 4.2, TMS-008, Sigma–Aldrich, Germany) aqueous solution for 5 min and rinsed twice with dH_2O. After that, images of the samples were captured under a stereomicroscope. To quantify the formation of the mineralized nodules, 10% cetylpyridinium chloride (6004–24-6, Sigma–Aldrich, USA) in 10 mM Na_3PO_4 (342483, Sigma–Aldrich, USA) was used to dissolve the red stains on TLM samples, and the absorbance was read at 630 nm.

Inflammatory Response and Capsulation of TLM Samples with Ag PIII Treatment in vivo

The surgical procedure and sampling are as follows: Eight-week-old male Sprague Dawley rats (SD rats, specific pathogen-free) were obtained from the Lab Animal Centre of Fourth Military Medical University, and 9 rats (180–220 g in weight) were used in this study. The rats were housed with free access to water, food and chewing materials under light/dark (12 h/12 h) cycles. Before the surgery, all rats were administered pentobarbital sodium (10 mg/100 g body weight, P3761, Sigma–Aldrich, USA) intraperitoneally for general anesthesia and articaine hydrochloride and epinephrine tartrate injection (Primacaine, France) for local anesthesia. Four incisions along the spine and following openings in the muscle sheath were made on the shaved back skin of each rat. Then, 3 groups of TLM samples were inserted randomly (each rat had 4 samples in 3 groups, one group had 2 samples), and all surgical incisions were sutured and applied with 1% erythromycin ointment (H44023088, Baiyunshan Pharma, China). After surgery, intramuscular injection of gentamicin sulfate (5000 U/kg/day) and administration of ibuprofen (H200319, Southwest Pharma, supplied in drinking water) were applied to all rats for 3 days to prevent infection and relieve pain post-surgery. Fourteen days after surgery, the rats were sacrificed by carbon dioxide (CO_2) inhalation, and the TLM samples with encapsulated tissue were removed as a whole part. The samples were rinsed three times in cold PBS and fixed in 4% paraformaldehyde for 36 h.

For histological observation and immunofluorescence staining, the TLM samples were carefully removed, and tissue attached to the TLM surfaces was collected. After dehydration in a series of ethanol solutions (30, 50, 70, 90, 95, 100, and 100%) and xylene (534056, Sigma–Aldrich, USA), tissue samples were embedded in paraffin and then sectioned (8 μm in thickness). To observe the morphology and measure the thickness of the fibrous encapsulation under a light microscope, the sections were stained with hematoxylin and eosin (HE staining). For immunofluorescence staining for tissue inflammatory infiltration, sections were first incubated at 60°C for 40 min for deparaffinization. Then, the sections were rehydrated in xylene and a series of ethanol solutions (100, 100, 95, 90, 70, 50, 30, 0%). The antigen retrieval of sections was conducted with 10 mM citric acid buffer (pH = 6.0, W230618, Sigma–Aldrich, USA) at 60°C overnight. After blocking with 1% BSA buffer, the sections were incubated with mouse anti-rat CD68 monoclonal antibody (1:25, MCA341, Bio-Rad, USA) at 4°C overnight. After rinsing three times with PBS, Alexa Fluor™ 568-labeled goat anti-mouse IgG (1:1000, A-11031 Invitrogen, USA) was applied to the sections for 1 h at RT, followed by nuclear counterstaining with DRAQ5 (1:800, 62251, Thermo Scientific, USA) for 5 min. After washing thrice with PBS, the sections were mounted with 50% glycerol and observed under LSCM. The thickness of fibrous capsulation was measured by Image-Pro plus 6.0 software (IPP 6.0, Media Cybernetics, USA). The $CD68^+$ macrophages were labeled/counted by ImageJ software.

Statistics

Experiments were repeated three times, with three to four replicates in each group. All data were plotted and analyzed using Prism 9.5.1 software (GraphPad Software, USA). All data are expressed as the mean ± standard deviation (SD) for continuous variables. Significant differences between groups were identified using one-way analysis of variance (ANOVA) followed by a Student-Newman–Keuls post hoc test for parametric data or a Kruskal–Wallis test followed by Dunn's multiple comparison tests for nonparametric data. Differences were considered statistically significant when $p < 0.01$. The detailed level of significance is also provided in the legends of figures and tables.

Results and Discussion

In this study, the samples were denoted as follows: polished TLM (TLM), anodized TLM (SNT), and anodized TLM samples with plasma immersion ion implantation (PIII) treatment (SNT Ag), as detailed in Table 1. Figure 1 illustrates the formation of a TiO_2 nanotubular array[39] on the TLM surface after anodization, with a tube length of 306.23 ± 15.64 nm, a diameter of 111.67 ± 7.55 nm, and a wall thickness of 24.52 ± 2.89 nm. Compared to the TiO_2 nanotubular array on a pure titanium (PT) surface, the nanotubes on the TLM surface were sparsely distributed,[33] providing increased inter-tubular space for accommodating the silver layer. After Ag PIII treatment, the SEM image of SNT Ag revealed thicker and blunter nanotube walls (diameter: 141.09 ± 9.93 nm, wall thickness: 45.16 ± 9.50 nm). Moreover, the lateral profile

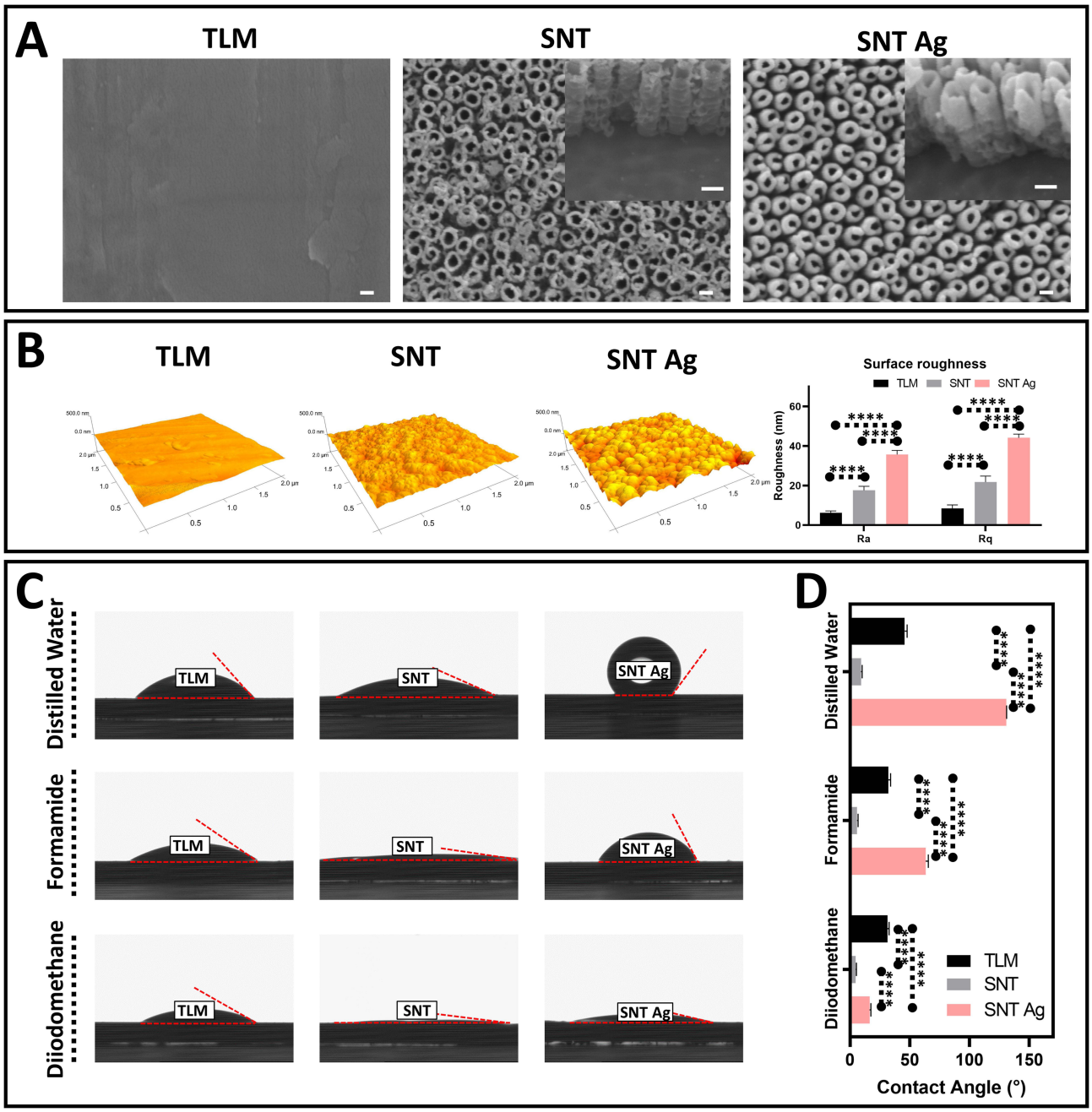

Figure 1 Surface characterization of TLM, SNT and SNT Ag surfaces. (**A**) Representative FE-SEM images of TLM, SNT and SNT Ag surfaces. Inserts, the profiles of TiO_2 nanotube array; (**B**) Representative AFM images and roughness measurement of TLM, SNT and SNT Ag surfaces; (**C** and **D**) Contact angles and wettability measurement of different solvents on TLM, SNT and SNT Ag surfaces. **** $p < 0.0001$; Scale bar = 100 nm.

of the SNT Ag nanotubes indicated an Ag-incorporated layer with a thickness of 153.21 ± 35.66 nm (Figure 1A). It is noteworthy that the SNT Ag surface exhibited a slightly darker color after Ag PIII, possibly due to superficial oxidation of the Ag layer, posing potential aesthetic concerns for future clinical applications, particularly in the context of transgingival abutments for dental implants.

AFM provided insights into the surface nanotopography of the samples (Figure 1B). Anodization significantly increased the surface roughness (measured as Ra and Rq), with further roughening observed after Ag PIII. The thicker tube walls smoothed top-tube edges after PIII, and larger intertubular space likely contributed to these results. Compared to the polished TLM surface, anodization enhanced the surface wettability of SNT for various solvents (dH_2O, formamide, and diiodomethane). However, Ag PIII reversed this enhancement. Figure 1C and D, and Table 2 illustrate that the total surface energy of SNT increased from 56.46 mJ/m^2 to 70.69 mJ/m^2 after anodization. Subsequently, the surface energy of SNT Ag decreased to 57.94 mJ/m^2 after Ag PIII treatment. It was reported that surface wettability could be an influential factor for cell and bacteria adhesion.[45] The hydrophobic surfaces have been reported to deter bacterial adhesion and promote bone cell growth.[45–48] Therefore, it can be inferred that the SNT Ag surface may not be conducive to bacterial growth while promoting the biofunctions of osteoblastic lineage cells.

To measure the change in Ag content on the SNT Ag surface, XPS with an ion beam etching assay was employed for step scanning. Figure 2A and Figure 2S (high-resolution) illustrate the alterations in $Ag3d_{5/2}$ (Figure 1SA), Ti2p (Figure 1SB), and O1s (Figure 1SC) content at various surface depths. Both TLM and SNT surfaces exhibited increased Ti and decreased O content with depth. SNT showed a higher O/Ti ratio due to the presence of the TiO_2 layer. On the top part of the Ag PIII layer on the SNT Ag surface, the Ag content exceeded 30 at% and then decreased gradually to approximately 5 at% at a depth of 150 nm. Notably, the Ag content rapidly increased in the top 4 nm (25.44 to 38.71 at%, Figure 2). In contrast, the O content dropped from 64.8 to 53.8 at%, indicating that the superficial Ag layer might be oxidized in air, as observed in previous studies.[49,50] In our previous work on a pure Ti surface, a low implantation voltage (0.5 Kv) led to more Ag deposition on the top 20 nm layer but with a shallower implantation depth (<5 at% at 50 nm in depth) compared with the higher implantation voltage in the present work.[51] Similarly, Ag PIII at a voltage ≤1.0 Kv on the SNT surface resulted in the superficial deposition of the Ag layer, blocking the nanotubes orifices (data not shown). Figure 2B depicts the elastic modulus measurement. The polished TLM and SNT samples exhibited differing elastic moduli with depth. On the TLM surface, the elastic modulus sharply increased to 165.10 GPa at a depth of 6.63 nm and then decreased to approximately 70 GPa at a depth of 400 nm (Figure 2SA). SNT and SNT Ag showed a similar gradual increase in elastic modulus with depth, indicating that anodization could form a softened surface. However, the elastic modulus of the SNT surface increased to 10.16 GPa at a depth of 81.93 nm, while that of SNT Ag reached 10.30 GPa at 24.03 nm (Figure 2SB and C). Ag PIII seemed to enhance the stiffness of the TiO_2 nanotube array. The elastic modulus of cortical and trabecular bone was reported to be 16.6~25.7 GPa and 13.4~19.4 GPa, respectively.[52] A matching elastic modulus between the bone tissue and implant material surface can significantly prevent stress shielding, which benefits the formation and stability of the implant-osseointegration interface. The Ag release dynamics were investigated using ICP-MS (Figure 2C). The cumulative Ag^+ concentration was detectable after 24 h (0.235 ± 0.02 ppm, ~2.20×10^{-9} M in 5 mL PBS) of incubation and rapidly increased within the first 7 days. Subsequently, Ag release slowed and reached a relative plateau (1.345 ± 0.12 ppm, ~1.20×10^{-8} M on day 30 in 5 mL PBS). The release of Ag^+ may confer potential antibacterial activity on the PIII-modified TLM implant.

Table 2 Solvent Contact Angles and Surface Energy of TLM, SNT and SNT Ag Surfaces

Group	Contact Angle (°)			Surface Energy (mJ/m^2)		
	Distilled H_2O	Formamide	Diiodomethane	Disperse	Polar	Total
TLM	48.50 ± 2.08	32.10 ± 1.93	31.30 ± 1.44	41.63	14.84	56.46
SNT	9.30 ± 0.89*	6.00 ± 0.7*	4.80 ± 0.63$^{\#}$	46.67	24.03	70.69
SNT Ag	130.90 ± 0.26*$^{\#}$	63.40 ± 2.22*$^{\#}$	16.50 ± 0.95*$^{\#}$	53.28	4.66	57.94

Notes: *p < 0.01 vs TLM, $^{\#}p$ < 0.01 vs SNT.

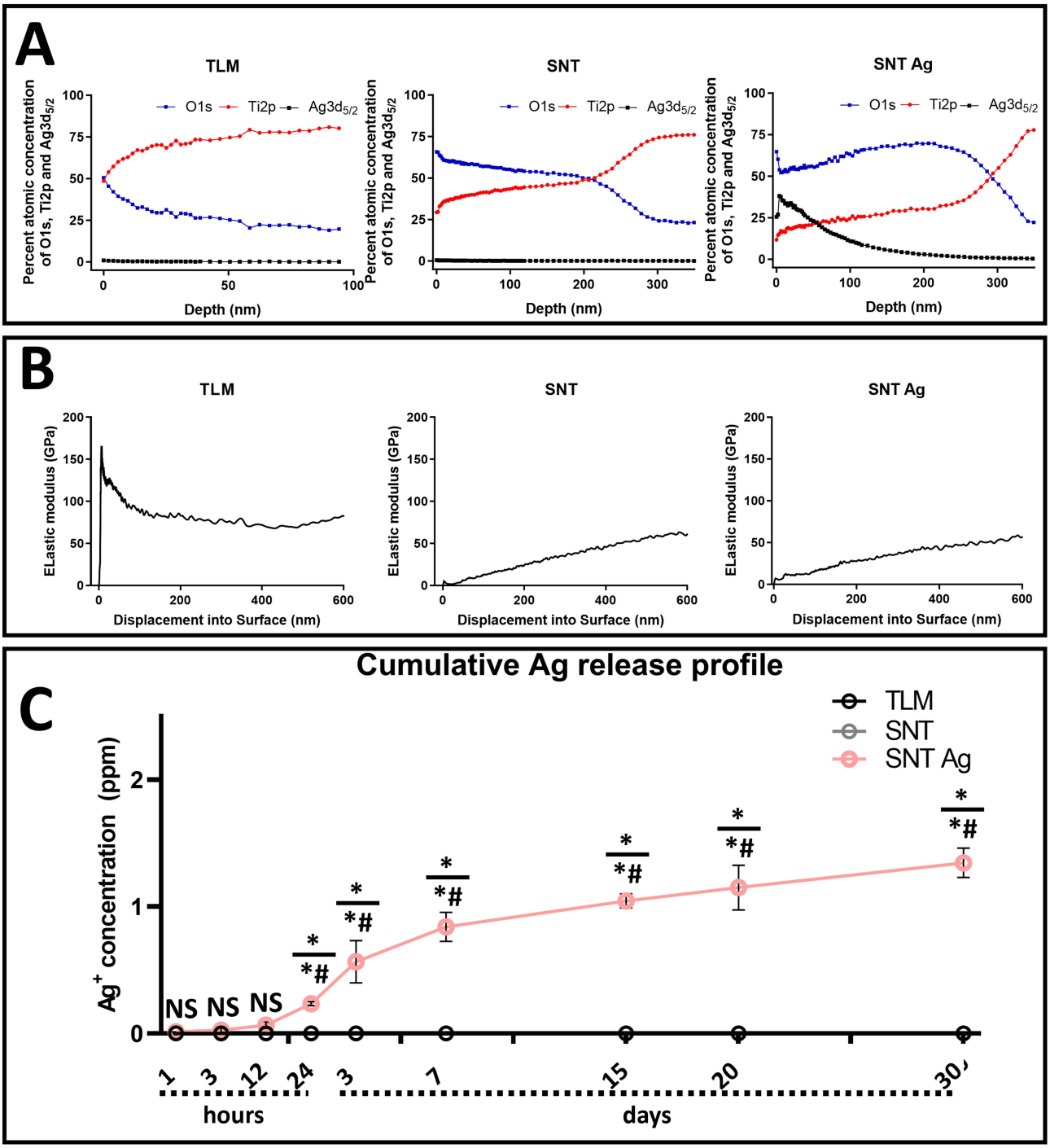

Figure 2 Ag distribution and release dynamics of TLM, SNT and SNT Ag surfaces. (**A**) Atomic percentage of O, Ti and Ag with depth by XPS; (**B**) Elastic modulus of TLM surfaces with depth by NanoIdenter; (**C**) Ag release dynamics (0–30 days) from TLM, SNT and SNT Ag surfaces by ICP-MS. $\frac{*}{*\#} = \frac{\text{SNT Ag vs TLM}}{\text{SNT Ag vs TLM \& SNT}}$, $p<0.01$; NS, no significance.

SA is considered the leading cause of tissue infection involving a variety of bone and soft tissues, with over one-third of implantable device-related infections attributed to SA.[53,54] Therefore, anti-SA activity is crucial for early survival and long-term stability of endosseous implants. The present study applied a direct contact assay to assess the antibacterial activity of TLM, SNT, and SNT Ag surfaces. Figure 3A illustrates different growth patterns and morphologies of SA on various surfaces at different time points. After 3 h of culture, SA exhibited similar distribution and density on all three surface groups. However, SA on the SNT Ag surface exhibited a crumpled cell wall with cracks and shrinkage. The

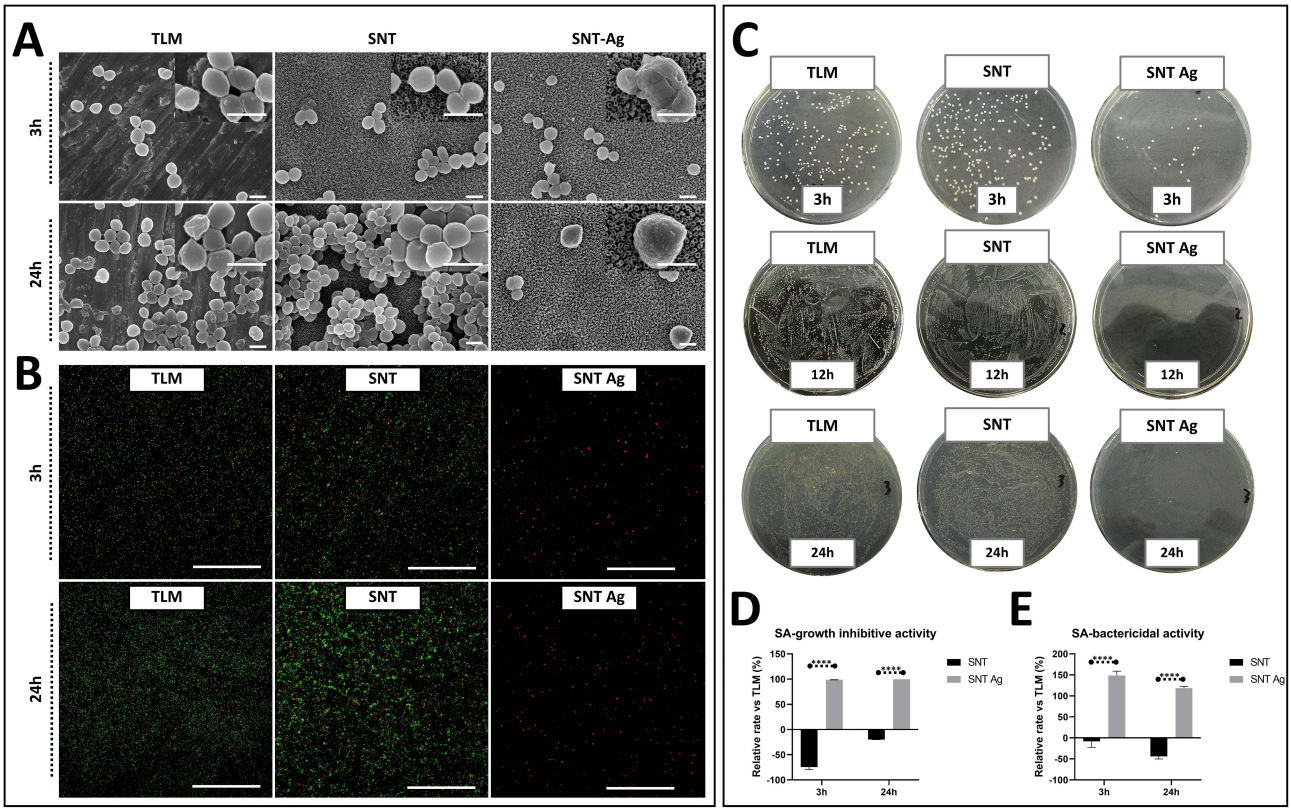

Figure 3 Antibacterial activity of TLM, SNT and SNT Ag surfaces. (**A**) Representative FE-SEM images of S. aureus (SA) growth on TLM, SNT and SNT Ag surfaces, scale bar = 1 μm; (**B**) Representative confocal images of live/dead SA on TLM, SNT and SNT Ag surfaces, scale bar = 100 μm; (**C**) Colony generation of SA on TLM, SNT and SNT Ag surfaces; (**D** and **E**) Growth inhibitive (**D**) and bactericidal (**E**) activity of SNT and SNT Ag surfaces based on confocal images, TLM was normalized as 100%. **** $p < 0.0001$. NS, no significance.

bactericidal effects of SNT Ag became more evident after 24 h. Compared to the well-proliferated SA with intact cell walls on TLM and SNT surfaces, only a few swollen SA were observed on the SNT Ag surface, with crumpled and damaged cell walls. The SYTO9/PI staining assay (Figure 3B) provided a straightforward way to distinguish live and dead bacteria on implant surfaces. TLM and SNT surfaces showed similar bacterial growth patterns, and SNT was found to increase SA proliferation (intense green signal on the SNT surface at 24 h). Conversely, only a few SYTO9-labelled SA cells were detected on SNT Ag surfaces, and the SYTO9/PI fluorescent signals ratio was obviously lower than that on TLM and SNT surfaces. The colony formation assay (based on sample elutes) was conducted to evaluate further the viability of SA attached to different surfaces. In Figure 3C, less proliferative SA was found in SNT Ag elutes compared to TLM and SNT elutes at 3 h. After 12 and 24 h of culture, almost no SA colonies formed in the SNT Ag group, while a large number of SA colonies formed in the TLM and SNT groups. In the present study, the antibacterial activity of different TLM samples was categorized into inhibitory and bactericidal activities (Figure 3D and E). Compared with TLM (Control, set as 100%), SNT increased SA proliferation at both time points (−74.49 ± 4.83% at 3 h and −19.92 ± 0.09% at 24 h) with negative bactericidal activity (−8.20 ± 14.32% at 3 h and −43.92 ± 6.14% at 24 h). In contrast, Ag PIII treatment (SNT Ag) almost entirely inhibited SA growth and exhibited over 2-fold bactericidal activity compared with TLM. Considering that the killed SA might detach from the SNT Ag surface, the potential bactericidal activity of SNT Ag could be higher than expected. Ning et al[30] reported that Ag^+ exhibited significant antibacterial (anti-SA) activity at concentrations starting from 10^{-7} M (~85% efficacy) and killed 99% SA at a concentration of 2.5×10^{-6} M. However, the Ag^+ released from the SNT Ag sample in 1 mL medium at 24 h was estimated to be 1.1×10^{-8} M, much lower than the reported Ag^+antibacterial threshold.[31] Therefore, the observed antibacterial activity of SNT Ag may be attributed to direct contact between bacteria and the Ag layer.

Although the antibacterial mechanisms of Ag and Ag^+ have not been fully understood, the scientific community formed four main consensuses. 1) Binding with sulfhydryl proteins to inactive specific proteins with dephosphorylation: Protein phosphorylation exists in several physiological processes of bacteria and is crucial for their signal transduction.[55] Ag nanoparticles were reported to anchor on the bacterial membrane and enter the bacteria to dephosphorylate the tyrosine residues of proteins, thereby inhibiting the activity of various bacterial enzymes and disrupting related bacterial behaviors.[56,57] 2) Disturbing the permeability of the bacterial membrane after Ag contacts the bacterial wall: The membrane of bacteria is rich in enzymes and proteins, which are essential for bacterial metabolism. The physiological functions of bacteria are hampered once the structural integrity of the bacterial membrane is impaired. Morones et al reported that Ag nanoparticles bond to the bacterial membrane via a high affinity of Ag^+ to the thiol group of membrane proteins (proteins containing sulfhydryl groups), leading to the deactivation and degradation of target membrane proteins, followed by the formation of irregular pits or holes on the outer layer of the bacterial membrane.[58] Through the injured membrane, the released Ag^+ further disrupts bacterial division and causes the bacterial plasma membrane to shrink and peel off from the cell wall.[59] 3) Disrupt the respiratory chain and lead to oxidative stress: Ag^+ was reported to bind to enzymes and destroy the dehydrogenase of the respiratory chain, thereby leading to an imbalance in the transmembrane proton pump and inhibiting bacterial metabolism.[60,61] The instability of the proton concentration inside and outside of the membrane hinders the transfer of electrons. In such an environment, oxygen is forced to accept electrons, which leads to synthesizing harmful ROS species.[61] Moreover, due to the high affinity of Ag^+ to thiols and selenol groups, Ag^+ was also found to disturb the ROS scavenging system, resulting in abnormal ROS regulation.[62] 4) Interfering with DNA replication: Through the damaged cell wall, Ag^+ can freely enter the bacteria and induce the DNA into a condensed form, thereby blocking DNA replication inside bacteria and giving rise to the death of bacteria.[63] Since bacteria can form a biofilm instantly after attaching to the implant surface, the diffusion of Ag^+ released from Ag PIII coatings may exhibit a distance-dependent restricted property. More concentrated Ag^+ was located near the SNT Ag surfaces and acted on attached SA. This may explain why SNT Ag exhibited an ideal anti-SA activity under such a low Ag^+ release concentration.

Addressing the high bactericidal activity of SNT Ag, whether the Ag PIII coating is cytocompatible is the first urgent question to be clarified in this study. L-929 cells were cultured either on the surfaces of TLM samples (contact assay) or in the extracts of TLM samples (extract assay). Figure 4A shows the L-929 morphology on different TLM samples. L-929 cells exhibited similar stretching on TLM and SNT surfaces but displayed a flatter morphology with a more extensive coverage on the SNT Ag surface. Neither contact nor extract assays showed any inhibition of SNT Ag regarding cell proliferation viability (MTT assay), as depicted in Figure 4B. Similarly, the LDH assay (Figure 4C) confirmed that the cell membrane integrity was not compromised after contact with the SNT Ag surface or its extracts over 30 days. It is noteworthy that the varying toxicities of Ag^+ on bacteria and eukaryotic cells at the same concentration could be an intriguing aspect to explore. Christina et al reported that Ag^+ started to show toxicity in human bone marrow mesenchymal stem cells (hBMSCs) at a concentration of 2.5 ppm,[32] which was 2-fold higher than the Ag^+ concentration in the SNT Ag extracts at 30 days (Figure 2C). Another possible explanation could be that eukaryotic cells cannot form extracellular matrix instantly upon attachment to the SNT Ag surface, thereby not restricting the diffusion of released Ag^+. Consequently, the Ag^+ concentration was unlikely to increase to the toxic level in the local milieu.

The osteogenic activities of TLM implants with Ag PIII treatment were assessed using osteoblastic MG-63 cells. Firstly, the morphology of osteoblastic MG-63 cells was analyzed using phalloidin and DRAQ5 staining. Figure 5A illustrates different cell morphologies on various TLM samples. In a proliferative environment (GM), MG-63 cells stretched and distributed evenly on the TLM surface. In contrast, on SNT and SNT Ag surfaces, cells tended to form aggregated multicellular structures, especially on the SNT Ag surface. Although cell density increased over time (over 80% confluency on day 7), SNT surfaces appeared to have fewer cells than TLM surfaces. In contrast, the spreading of MG-63 on the SNT Ag surface was much lower than that on the TLM and SNT surfaces, and all cells exhibited rounded shapes. After being cultured on SNT Ag for 3 days, the cell density increased obviously but still with less stretching. MG-63 cells showed a prominent structure of "a bunch of grapes", indicating that MG-63 on the SNT Ag surface may suffer from poor spreading, which may be attributed to undesirable focal adhesion formation. However, MG-63 cells reached over 90% confluency on day 7, suggesting cell proliferation was not hampered on the SNT Ag surface.

On the other hand, MG-63 cells on the SNT Ag surface showed different behaviors in OM (osteogenic differentiation environments). Compared to GM, OM promoted cell growth in all three groups. MG-63 cells on the TLM and SNT

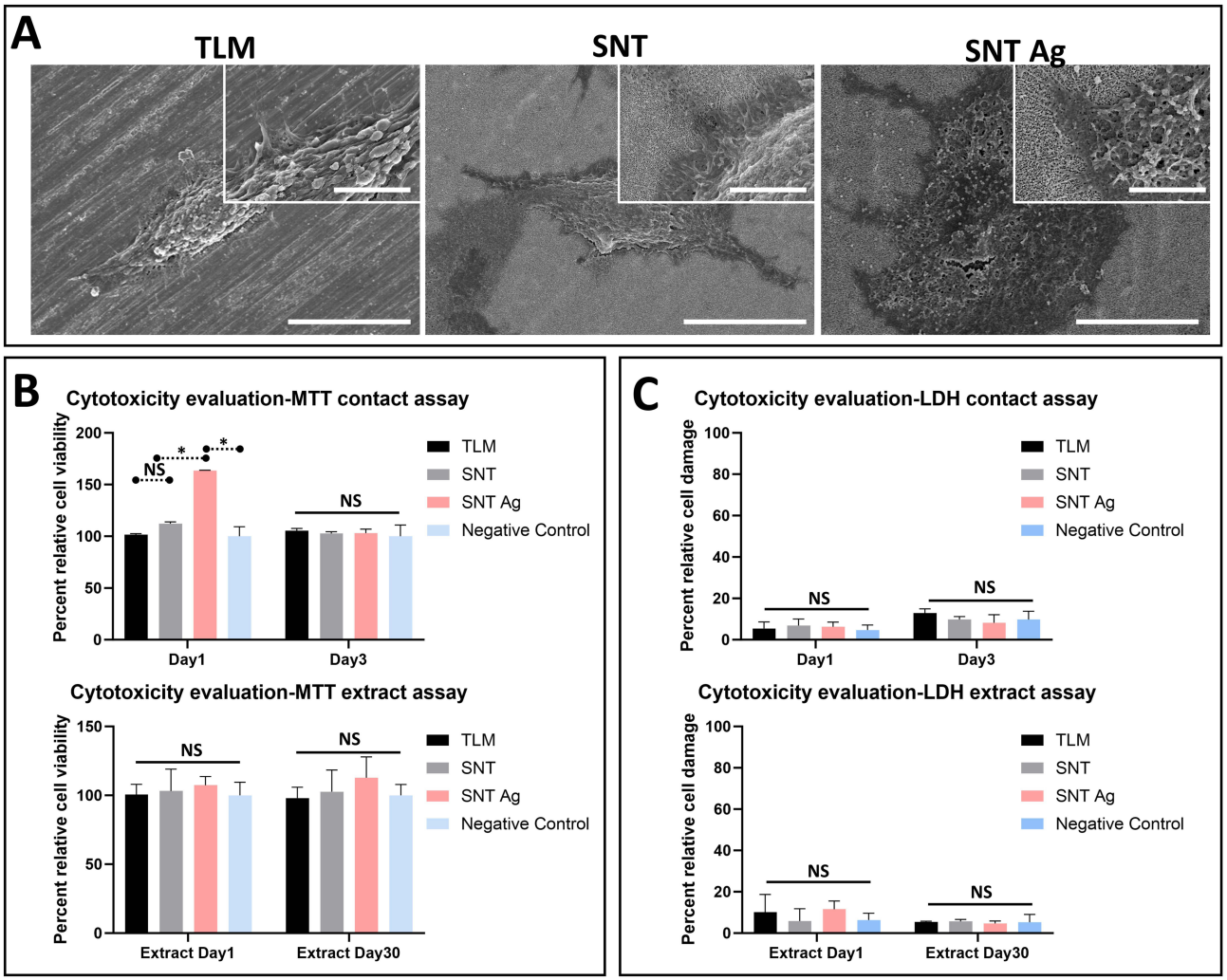

Figure 4 Cytocompatibility of TLM, SNT and SNT Ag surfaces. (**A**) Representative FE-SEM images of mouse L-929 fibroblasts on TLM surfaces with detailed inserts; (**B** and **C**) MTT-based (**B**) and LDH-based (**C**) cytotoxicity evaluation, Upper row, contact assay; Lower row, extract assay; *$p < 0.05$. NS, no significance. Scale bar = 5 μm.

surfaces showed similar morphology and growth behavior but with an obviously higher cell density after day 3. Strikingly, the attachment and stretching of cells were dramatically improved on the SNT Ag surface. MG-63 cells showed clear F-actin stretching bundles and a multilayered, cross-linked cell network on the SNT Ag surface after Day 3. These results suggest that MG-63 cells were able to overcome the spreading inhibition of the SNT Ag surface, potentially due to enhanced extracellular matrix (ECM) production. There was no difference in cell proliferation on different surfaces in GM on Day 1 (Figure 5B). SNT Ag slightly enhanced the proliferation viability compared with the polished TLM surface on Day 3, but such enhancement vanished on Day 7. The SNT surface was shown to inhibit MG-63 proliferation on Day 7. Similarly, MG-63 cells had no difference in proliferation on different surfaces in OM on Day 1, and enhanced proliferation could also be observed on the SNT Ag surface on Day 3. Intriguingly, OM reversed the proliferation inhibition of the SNT surface and further promoted proliferation on the SNT Ag surface, consistent with the confocal images described above.

Cell adhesion is significantly influenced by surface roughness and hydrophilicity. Dowling et al and Wang et al reported that a rougher surface (NT with nanotube size of 80 nm) led to higher cell attachment but limited spreading.[64,65] The nano-topography of SNT and SNT Ag surfaces likely contributed to differences in attachment and spreading. According to the classic models of Young, Wenzal and Cassie-Baxter, even with similar hydrophobic surface properties, the starting shapes of water droplets differed on smooth surfaces and spike-array-like surfaces.[66] The spike-like array

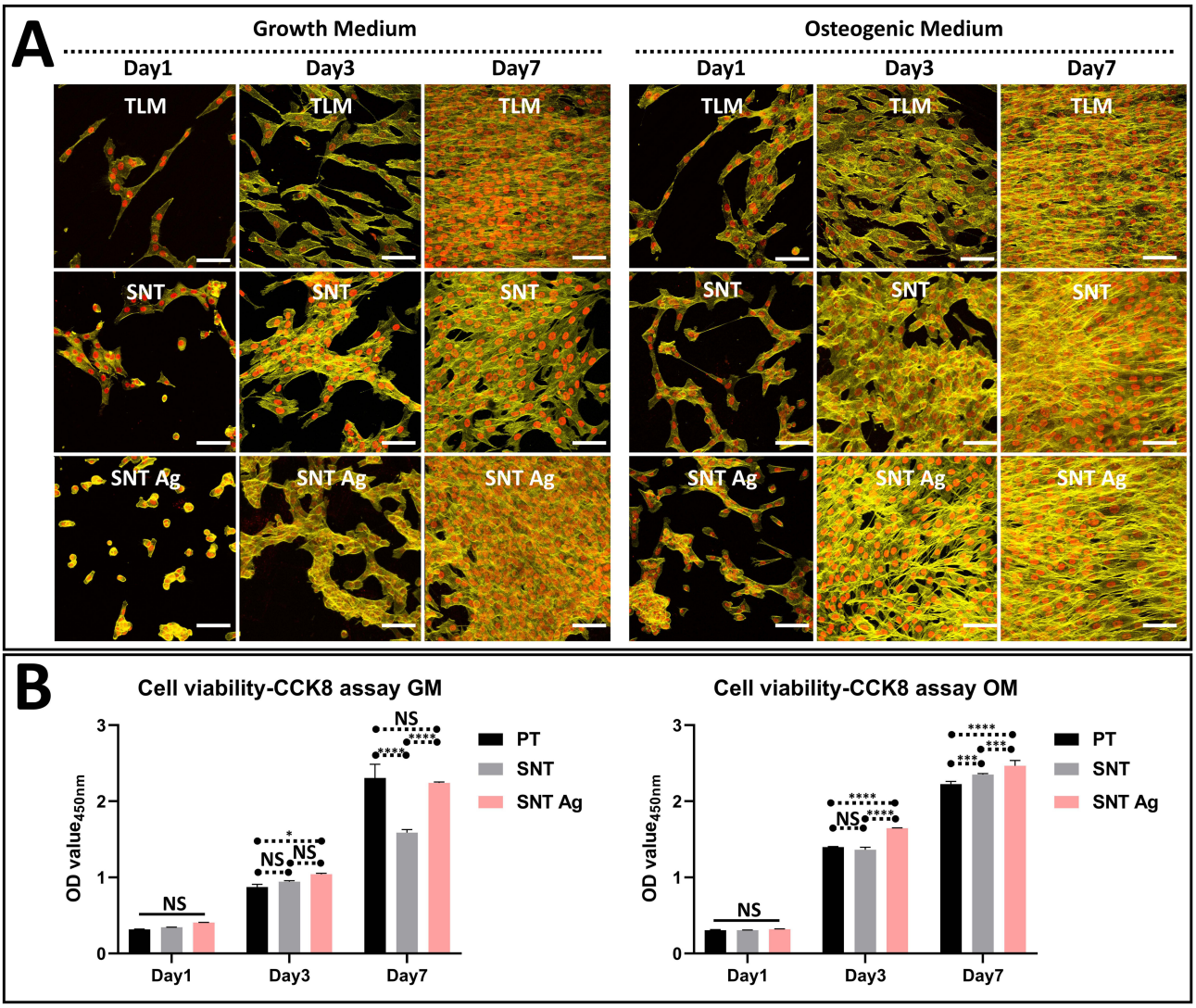

Figure 5 Morphology of human osteoblastic MG-63 cells on TLM, SNT and SNT Ag surfaces in different culture media. (**A**) Representative FE-SEM images of MG-63 cells in growth medium (GM, left column) and osteogenic medium (OM, right column); (**B**) CCK8-based cell viability evaluation in GM and OM; *$p < 0.05$, *** $p < 0.001$, **** $p < 0.0001$. NS, no significance. Scale bar = 100 μm.

surface maintained high hydrophobicity since fine needle arrays trapped air under the droplet between the surface projections.[66] The entrapped air neither supported cell adhesion nor provided nourishing space for cell growth. However, a hydrophobic implant surface was prone to have higher protein adsorption than a hydrophilic surface.[67–69] Another study reported similar amounts of protein adsorption regardless of whether a surface is hydrophobic or hydrophilic.[70] Interestingly, after incubating in a culture medium with 10% FCS for 60 min, the SNT Ag surface showed obvious hydrophilicity (Figure 3S). In the OM culture environment, MG-63 cells were induced to synthesize hydrophilic ECM proteins[71–73] on top of the nanotubes, further enhancing the hydrophilicity of the SNT Ag surface and providing a favorable environment for cell spreading.[74] Moreover, the thickened top edge of TiO_2 nanotubes after PIII treatment also contributed to a larger area for cell growth compared to SNT. It is important to note that currently available commercial implants exhibit superior clinical performance concerning hydrophilicity, indicating shorter healing time and enhanced osseointegration (eg, Straumann SLActive).[75]

A PCR array technique was employed in this study to obtain a broad pattern of osteogenic gene expression. The expression of each gene in the TLM at different times was normalized to 1.0 as a control. The relative expression levels of SNT and SNT Ag were calculated with the $\log_2$ function. Figure 6A depicts the osteogenic gene expression profile in

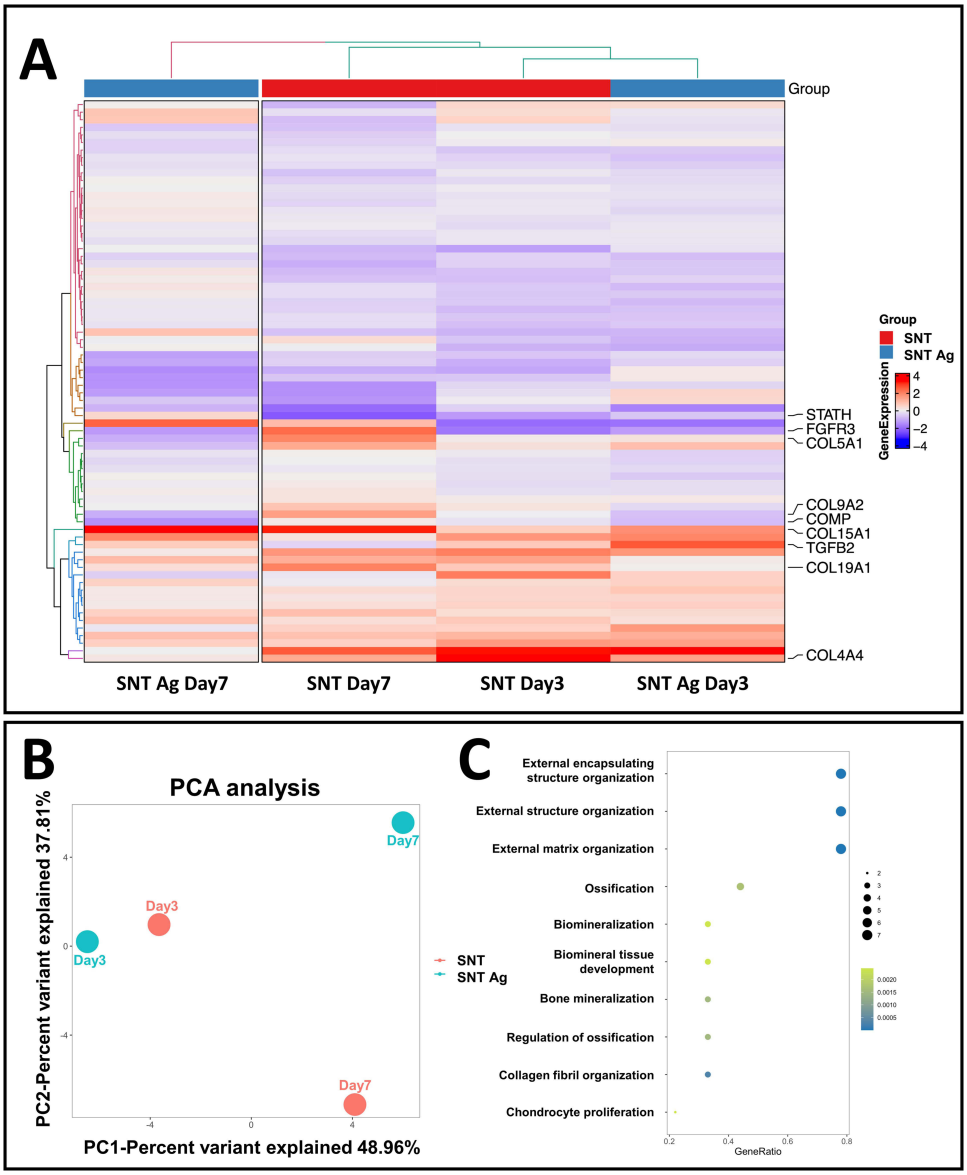

Figure 6 Osteogenic genes expression profile of MG-63 cells on TLM, SNT and SNT Ag surfaces at Day3 and Day7. (**A**) Heatmap and cluster analysis of osteogenic genes expression in MG-63 cells; (**B**) Principal Component Analysis; (**C**) Gene ontology (GO) biological process analysis. Dot size, number of genes classified; Color bar, statistical significance.

MG-63 cells on SNT and SNT Ag on Day 3 and Day 7. In general, SNT and SNT Ag shared similar osteogenic gene expression patterns. However, some genes, such as STATH and FGFR3, etc., showed different expression levels. Cluster analysis classified SNT Day3 and SNT Ag Day3 as one group. At the next grouping level, SNT Day7 could also be considered one group with SNT Day3 and SNT Ag Day3. In contrast, SNT Ag Day7 was not considered in the same group as any other samples. The PCA provided a more summarized conclusion (Figure 6B). On the first principal component (PC1), the Day 3 and Day 7 time-point groups could be significantly distinguished, and the difference between the treatment groups at different times was noticeable. In contrast, the difference within each time-point group was slight. On PC2, the difference between SNT and SNT Ag on Day 3 was not noticeable, whereas SNT and SNT Ag on Day 7 exhibited a significant difference. Such results indicated that SNT and SNT Ag had similar osteogenic gene expression patterns on Day 3, but such similarity vanished with time. Figure 6C summarizes the genes with the most apparent differential expression among different groups. It classifies their functions through GO biological process analysis, mainly locating the functions of ECM synthesis, collagen fiber organization, and biomineralization. Although

previous work has proven that osteogenic genes (*ALP. RUNX2, COL1A1, BMP-2, OPN, OCN*) expression in primary osteoblastic lineage cells could be improved by both TiO_2 nanotubes (NT) on a pure Ti surface and SNT on a TLM surface,[35,39] the present study demonstrates for the first time that Ag PIII implantation technology can alter the pattern of long-term osteogenic gene expression in cells by slightly changing the SNT surface topography. As the culture media were changed every 2 days, the cumulative Ag^+ was unlikely to reach a level that could affect the osteogenic differentiation of MG-63 cells. ECM mineralization assays were conducted to study further the effects of Ag PIII treatment on macroscopic ECM synthesis and mineralization. Figure 7A demonstrates that ALP production was solely promoted on the SNT Ag surface. The SNT surface improved mineralized nodule formation and collagen secretion, further enhanced after Ag PIII treatment. Semiquantitative analysis of ARS and Sirius Red staining also supported these findings (Figure 7B and C). Qin et al also reported that stainless steel dramatically promoted the osteogenic differentiation of hBMSCs after PIII treatment without detectable Ag^+ release,[76] indicating that elemental Ag implanted on the biomaterial surface, rather than the released Ag^+, can effectively promote host osteogenesis. Moreover, the size and form of elemental Ag are also crucial for their biological functions. Nanoscaled Ag particles can be easily captured by human osteoblastic lineage cells and agglomerated in endolysosomal cell compartments, which may affect cells adversely.[77] Nguyen and Sengstock et al reported that Ag nanoparticles with a size of 10–80 nm did not improve osteogenic differentiation at low concentrations (≤10 μg/mL) but impaired both adipogenic and osteogenic differentiation of hMSCs in a dose-dependent manner at high concentrations (≥20 μg/mL).[78,79] Therefore, Ag modification on the implant surface that can improve the osteogenic functions of bone tissue needs to meet the following requirements: 1) the lowest Ag content with effective antibacterial properties; 2) stable embedding on the implant surface; and 3) maintaining the original osteogenic surface topography on the implant.

Apart from host osteogenesis, unavoidable inflammatory responses after implantation were also crucial for the prognosis of implants. In our previous study, macrophage activation and M1/M2c polarization were directly mediated by the surface nanostructure of the implant.[80] The polarized macrophages could further control the osteogenic difference of hBMSCs in vitro and manipulated osteogenesis in vivo.[33,80] The trans-gingival site of the implant communicates with the oral cavity and is directly subjected to the invasion of bacteria.[81] Good connective tissue sealing can effectively maintain the stability of the

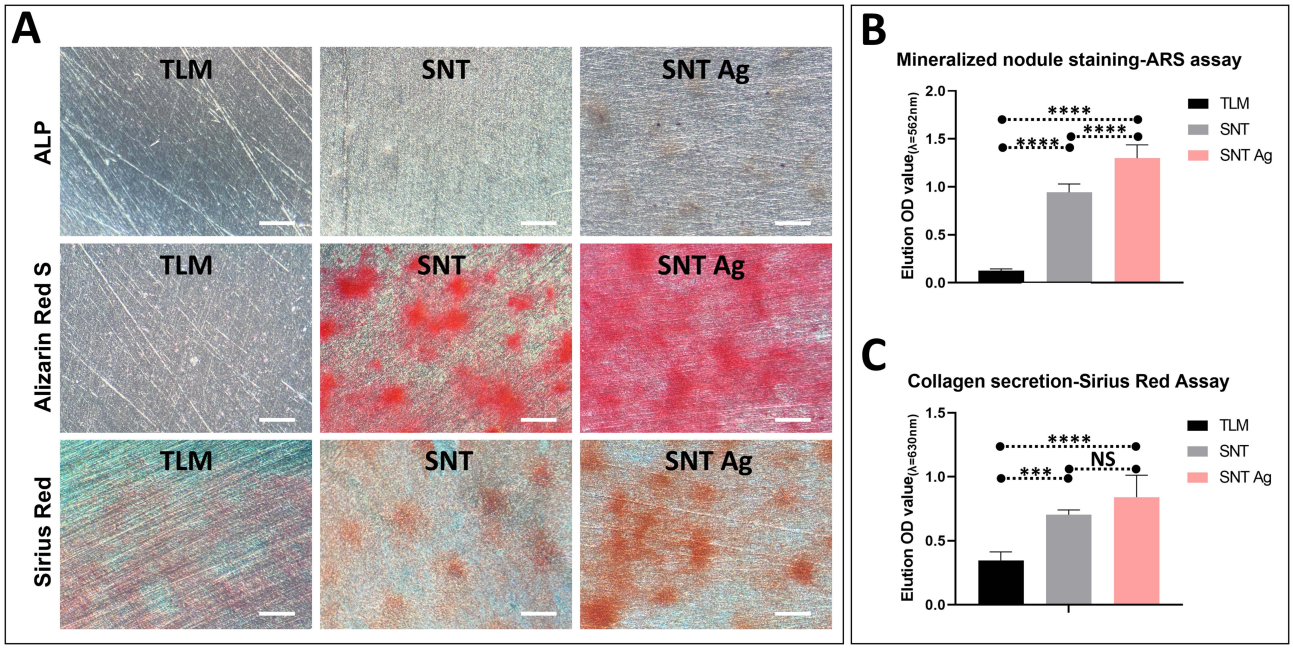

Figure 7 Macroscopic ECM mineralization of MG-63 cells on TLM, SNT and SNT Ag surfaces. (**A**) Representative images of ALP synthesis (top), mineralized nodule formation (middle), and collagen secretion (bottom) in MG-63 cells; (**B** and **C**) Semi-quantitative analysis of mineralized nodule formation (**B**) and collagen secretion (**C**) on TLM, SNT and SNT Ag surfaces; *$p < 0.05$, ** $p < 0.01$, *** $p < 0.001$, **** $p < 0.0001$. Scale bar = 1000 μm.
Abbreviation: NS, no significance.

microenvironment around the implant underneath.[82,83] Once tissue inflammation and hyperplasia occur at the trans-gingival site, gingival edema occurs, the epithelium grows excessively into the gingival sulcus, and the peri-implant gingival sealing is destroyed.[81] Therefore, it is most important to inspect the inflammatory response and capsulation of connective tissue around nanostructured TLM abutments with Ag PIII treatment. Figure 8A demonstrates that thick fibrous encapsulation formed

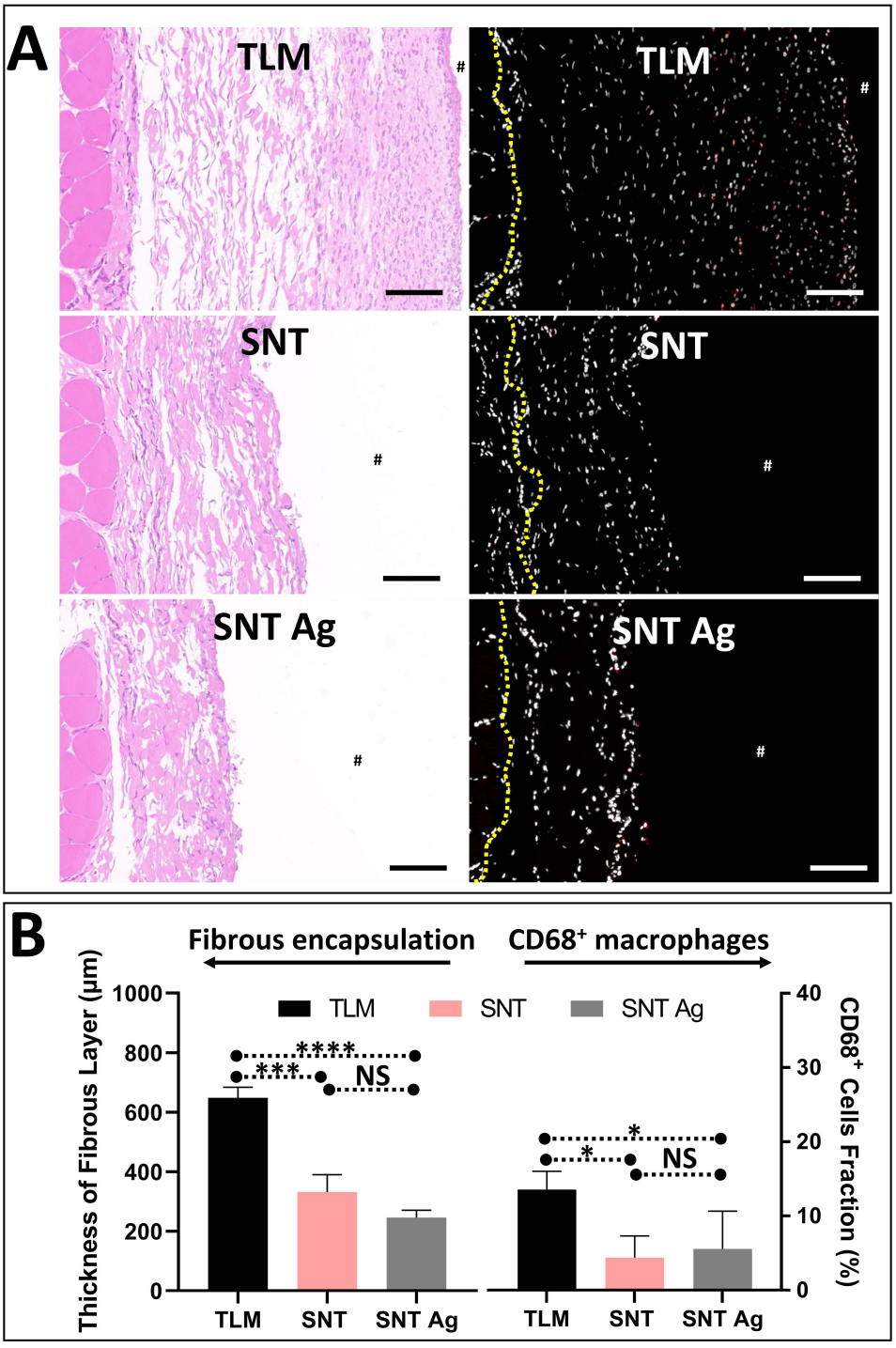

Figure 8 Soft tissue compatibility and inflammatory irritation of implants with TLM, SNT and SNT Ag surfaces in vivo. (**A**) Representative images of fibrous tissue encapsulation (HE staining, left panel) and $CD68^+$ macrophages activation (immunofluorescent staining, white: cell nuclei, Red: CD68) around TLM samples (#) 14 days post-implantation; (**B**) Quantitative analysis of fibrous encapsulation formation (Left panel) and fraction of $CD68^+$ macrophages (right panel). *$p < 0.05$, *** $p < 0.001$, **** $p < 0.0001$. Scale bar = 100 μm.

Abbreviation: NS, no significance.

around polished TLM implants with a thickness of over 600 μm. Such encapsulation consisted of two layers: a densified layer rich in collagen components with intense inflammatory infiltration and loose connective tissue underneath. The first layer in contact with TLM implants was characterized by partial epithelialization. CD68 fluorescence staining showed that the $CD68^+$ macrophages were mostly located in the densified inflammatory layer. However, such fibrous hyperplasia vanished around the SNT implant, and the proportion of $CD68^+$ macrophages also decreased significantly. Ag PIII treatment maintained similar CD68+ macrophage activation and slightly reduced fibrous encapsulation thickness around the SNT implant. Nevertheless, such a decrease was insignificant (Figure 8B). Along with soft tissue responses, osseointegration around the SNT Ag implant is crucial for future clinical applications. Achieving an ideal, evenly distributed Ag layer on an SNT cylinder implant remains challenging, requiring further optimization of Ag PIII parameters.

Conclusions

Sparsely distributed nanotube arrays incorporating stable Ag were successfully established on the TLM implant surface using PIII technology for the first time. This novel nanostructured implant surface, exhibiting robust antibacterial properties against Staphylococcus aureus and excellent cytocompatibility, also demonstrated remarkable osteogenic activities and mitigated inflammatory responses in vivo. These promising results highlight the potential application of this Ag-incorporated nanostructured surface for both trans-gingival abutments and endosseous implants. However, further investigations are imperative to assess the in vivo osseointegration of the SNT Ag implant and to address aesthetic concerns associated with Ag PIII modification.

Data Sharing Statement

The raw data required to reproduce these findings cannot be shared at this time as the data also forms part of an ongoing study. Data can be provided by the corresponding author, Qianli Ma, upon request after publication.

Ethics Approval and Consent to Participate

For the animal in vivo research: All animal experiments were conducted and supervised under the Ethical Approval (No. KY20194055) approved by the animal experiment ethics committee of the Fourth Military Medical University. All laboratory animals were taken cared according to the Guide for the Care and Use of Laboratory Animals of Fourth Military Medical University (2018). Consent to participate is not applicable.

Author Contributions

All authors made a significant contribution to the work reported, whether that is in the conception, study design, execution, acquisition of data, analysis and interpretation, or in all these areas; took part in drafting, revising or critically reviewing the article; gave final approval of the version to be published; have agreed on the journal to which the article has been submitted; and agree to be accountable for all aspects of the work.

Funding

The authors acknowledge financial support from the National Natural Science Foundation of China (NSFC, No. 81971752).

Disclosure

The authors report no conflicts of interest in this work.

References

1. Geetha M, Singh AK, Asokamani R, Gogia AK. Ti based biomaterials, the ultimate choice for orthopaedic implants - A review. *Prog Mater Sci*. 2009;54(3):397–425. doi:10.1016/j.pmatsci.2008.06.004
2. Hanawa T. Titanium-Tissue Interface Reaction and Its Control With Surface Treatment. *Front Bioeng Biotech*. 2019;7. doi:10.3389/fbioe.2019.00170
3. Romanos GE, Delgado-Ruiz R, Sculean A. Concepts for prevention of complications in implant therapy. *Periodontol*. 2019;81(1):7–17. doi:10.1111/prd.12278

4. Arciola CR, Campoccia D, Montanaro L. Implant infections: adhesion, biofilm formation and immune evasion. *Nat Rev Microbiol*. 2018;16(7):397–409. doi:10.1038/s41579-018-0019-y
5. Berglundh T, Armitage G, Araujo MG, et al. Peri-implant diseases and conditions: consensus report of workgroup 4 of the 2017 World Workshop on the Classification of Periodontal and Peri-Implant Diseases and Conditions. *J Periodontol*. 2018;89(Suppl 1):S313–S318. doi:10.1002/JPER.17-0739
6. Ertas K, Pence I, Cesmeli MS, Ay ZY. Determination of the stage and grade of periodontitis according to the current classification of periodontal and peri-implant diseases and conditions (2018) using machine learning algorithms. *J Periodontal Implant Sci*. 2023;53(1):38–53. doi:10.5051/jpis.2201060053
7. Schwarz F, Alcoforado G, Guerrero A, et al. Peri-implantitis: summary and consensus statements of group 3. The 6th EAO Consensus Conference 2021. *Clin Oral Implants Res*. 2021;32(Suppl 21):245–253. doi:10.1111/clr.13827
8. Mei SL, Wang HY, Wang W, et al. Antibacterial effects and biocompatibility of titanium surfaces with graded silver incorporation in titania nanotubes. *Biomaterials*. 2014;35(14):4255–4265. doi:10.1016/j.biomaterials.2014.02.005
9. Zhao LZ, Chu PK, Zhang YM, Wu ZF. Antibacterial Coatings on Titanium Implants. *J Biomed Mater Res B*. 2009:91.
10. Harris LG, Tosatti S, Wieland M, Textor M, Richards RG. Staphylococcus aureus adhesion to titanium oxide surfaces coated with non-functionalized and peptide-functionalized poly(L-lysine)-grafted-poly(ethylene glycol) copolymers. *Biomaterials*. 2004;25(18):4135–4148. doi:10.1016/j.biomaterials.2003.11.033
11. Campoccia D, Montanaro L, Speziale P, Arciola CR. Antibiotic-loaded biomaterials and the risks for the spread of antibiotic resistance following their prophylactic and therapeutic clinical use. *Biomaterials*. 2010;31(25):6363–6377. doi:10.1016/j.biomaterials.2010.05.005
12. Jepsen K, Jepsen S. Antibiotics/antimicrobials: systemic and local administration in the therapy of mild to moderately advanced periodontitis. *Periodontol*. 2016;71(1):82–112. doi:10.1111/prd.12121
13. Bormann N, Schwabe P, Smith MD, Wildemann B. Analysis of parameters influencing the release of antibiotics mixed with bone grafting material using a reliable mixing procedure. *Bone*. 2014;59:162–172. doi:10.1016/j.bone.2013.11.005
14. Hickok NJ, Shapiro IM, Chen AF. The Impact of Incorporating Antimicrobials into Implant Surfaces. *J Dent Res*. 2018;97(1):14–22. doi:10.1177/0022034517731768
15. Lei J, Sun LC, Huang SY, et al. The antimicrobial peptides and their potential clinical applications. *Am J Transl Res*. 2019;11(7):3919–3931.
16. Chen ST, Chien HW, Cheng CY, et al. Drug-release dynamics and antibacterial activities of chitosan/cefazolin coatings on Ti implants. *Prog Org Coat*. 2021;159.
17. Kazemzadeh-Narbat M, Lai BFL, Ding CF, Kizhakkedathu JN, Hancock REW, Wang RZ. Multilayered coating on titanium for controlled release of antimicrobial peptides for the prevention of implant-associated infections. *Biomaterials*. 2013;34(24):5969–5977. doi:10.1016/j.biomaterials.2013.04.036
18. Kligman S, Ren Z, Chung CH, et al. The Impact of Dental Implant Surface Modifications on Osseointegration and Biofilm Formation. *J Clin Med*. 2021;10(8):1641. doi:10.3390/jcm10081641
19. Zheng YH, Li JB, Liu XY, Sun J. Antimicrobial and osteogenic effect of Ag-implanted titanium with a nanostructured surface. *Int J Nanomed*. 2012;7:875–884.
20. Abdi M, Mirkalantari S, Amirmozafari N. Bacterial resistance to antimicrobial peptides. *J Pept Sci*. 2019;25(11). doi:10.1002/psc.3210
21. Jangir PK, Ogunlana L, Szili P, et al. The evolution of colistin resistance increases bacterial resistance to host antimicrobial peptides and virulence. *Elife*. 2023;12.
22. Wang G, Feng H, Hu L, et al. An antibacterial platform based on capacitive carbon-doped TiO(2) nanotubes after direct or alternating current charging. *Nat Commun*. 2018;9(1):2055. doi:10.1038/s41467-018-04317-2
23. Wang GM, Tang KW, Jiang WJ, et al. Quantifiable Relationship Between Antibacterial Efficacy and Electro-Mechanical Intervention on Nanowire Arrays. *Adv Mater*. 2023;35(19):e6.
24. Dehnavi AS, Raisi A, Aroujalian A. Control Size and Stability of Colloidal Silver Nanoparticles with Antibacterial Activity Prepared by a Green Synthesis Method. *Synth React Inorg M*. 2013;43(5):543–551. doi:10.1080/15533174.2012.741182
25. Kumar S, Singh M, Halder D, Mitra A. Mechanistic study of antibacterial activity of biologically synthesized silver nanocolloids. *Colloid Surface A*. 2014;449:82–86. doi:10.1016/j.colsurfa.2014.02.027
26. Suganya KSU, Govindaraju K, Kumar VG, et al. Size controlled biogenic silver nanoparticles as antibacterial agent against isolates from HIV infected patients. *Spectrochim Acta A*. 2015;144:266–272. doi:10.1016/j.saa.2015.02.074
27. Silver S. Bacterial silver resistance: molecular biology and uses and misuses of silver compounds. *Fems Microbiol Rev*. 2003;27(2–3):341–353. doi:10.1016/S0168-6445(03)00047-0
28. Mohammed ABA, Abd Elhamid MM, Khalil MKM, Ali AS, Abbas RN. The potential activity of biosynthesized silver nanoparticles of Pseudomonas aeruginosa as an antibacterial agent against multidrug-resistant isolates from intensive care unit and anticancer agent. *Environ Sci Eur*. 2022;34(1):56.
29. Franci G, Falanga A, Galdiero S, et al. Silver Nanoparticles as Potential Antibacterial Agents. *Molecules*. 2015;20(5):8856–8874. doi:10.3390/molecules20058856
30. Ning C, Wang X, Li L, et al. Concentration ranges of antibacterial cations for showing the highest antibacterial efficacy but the least cytotoxicity against mammalian cells: implications for a new antibacterial mechanism. *Chem Res Toxicol*. 2015;28(9):1815–1822. doi:10.1021/acs.chemrestox.5b00258
31. Agarwal A, Weis TL, Schurr MJ, et al. Surfaces modified with nanometer-thick silver-impregnated polymeric films that kill bacteria but support growth of mammalian cells. *Biomaterials*. 2010;31(4):680–690. doi:10.1016/j.biomaterials.2009.09.092
32. Greulich C, Braun D, Peetsch A, et al. The toxic effect of silver ions and silver nanoparticles towards bacteria and human cells occurs in the same concentration range. *Rsc Adv*. 2012;2(17):6981–6987. doi:10.1039/c2ra20684f
33. Ma QL, Zhao LZ, Liu RR, et al. Improved implant osseointegration of a nanostructured titanium surface via mediation of macrophage polarization. *Biomaterials*. 2014;35(37):9853–9867. doi:10.1016/j.biomaterials.2014.08.025
34. Wang JJ, Meng FH, Song W, et al. Nanostructured titanium regulates osseointegration via influencing macrophage polarization in the osteogenic environment. *Int J Nanomed*. 2018;13:4029–4043. doi:10.2147/IJN.S163956

35. Ma QL, Fang L, Jiang N, et al. Bone mesenchymal stem cell secretion of sRANKL/OPG/M-CSF in response to macrophage-mediated inflammatory response influences osteogenesis on nanostructured Ti surfaces. *Biomaterials*. 2018;154:234–247. doi:10.1016/j.biomaterials.2017.11.003
36. Fu YR, Jing Z, Chen T, et al. Nanotube patterning reduces macrophage inflammatory response via nuclear mechanotransduction. *J Nanobiotechnol*. 2023;21(1). doi:10.1186/s12951-023-01912-4
37. Ma QL, Mei SL, Ji K, Zhang YM, Chu PK. Immobilization of Ag nanoparticles/FGF-2 on a modified titanium implant surface and improved human gingival fibroblasts behavior. *J Biomed Mater Res A*. 2011:98.
38. Zhao LZ, Wei YP, Li JX, Han Y, Ye RD, Zhang YM. Initial osteoblast functions on Ti-5Zr-3Sn-5Mo-15Nb titanium alloy surfaces modified by microarc oxidation. *J Biomed Mater Res A*. 2010:92.
39. Mei SL, Zhao LZ, Wang W, Ma QL, Zhang YM. Biomimetic Titanium Alloy with Sparsely Distributed Nanotubes Could Enhance Osteoblast Functions. *Adv Eng Mater*. 2012;14(4):B166–B174. doi:10.1002/adem.201180056
40. Cao HL, Liu XY, Meng FH, Chu PK. Biological actions of silver nanoparticles embedded in titanium controlled by micro-galvanic effects. *Biomaterials*. 2011;32(3):693–705. doi:10.1016/j.biomaterials.2010.09.066
41. Owens DK, Wendt RC. Estimation of the surface free energy of polymers. *J Appl Polym Sci*. 1969;13(8):1741–1747. doi:10.1002/app.1969.070130815
42. Kaelble DH. Dispersion-Polar Surface Tension Properties of Organic Solids. *J Adhesion*. 1970;2(2):66–81. doi:10.1080/0021846708544582
43. International Organization for Standardization. *ISO 10993-5:2009 Biological Evaluation of Medical Devices. Part 5: Tests for in vitro Cytotoxicity*; 2009.
44. Berger E, Breznan D, Stals S, et al. Cytotoxicity assessment, inflammatory properties, and cellular uptake of Neutraplex lipid-based nanoparticles in THP-1 monocyte-derived macrophages. *Nanobiomedicine*. 2017;4:1849543517746259. doi:10.1177/1849543517746259
45. Kunrath MF, Leal BF, Hubler R, de Oliveira SD, Teixeira ER. Antibacterial potential associated with drug-delivery built TiOnanotubes in biomedical implants. *Amb Express*. 2019;9. doi:10.1186/s13568-019-0777-6
46. Lai Y, Huang J, Cui Z, et al. Recent Advances in TiO2 -Based Nanostructured Surfaces with Controllable Wettability and Adhesion. *Small*. 2016;12(16):2203–2224. doi:10.1002/smll.201501837
47. Fadeeva E, Truong VK, Stiesch M, et al. Bacterial retention on superhydrophobic titanium surfaces fabricated by femtosecond laser ablation. *Langmuir*. 2011;27(6):3012–3019. doi:10.1021/la104607g
48. Gittens RA, Scheideler L, Rupp F, et al. A review on the wettability of dental implant surfaces II: biological and clinical aspects. *Acta Biomater*. 2014;10(7):2907–2918. doi:10.1016/j.actbio.2014.03.032
49. Erol M, Han Y, Stanley SK, Stafford CM, Du H, Sukhishvili S. SERS Not To Be Taken for Granted in the Presence of Oxygen. *J Am Chem Soc*. 2009;131(22):7480–7481. doi:10.1021/ja807458x
50. Yin YD, Li ZY, Zhong ZY, Gates B, Xia YN, Venkateswaran S. Synthesis and characterization of stable aqueous dispersions of silver nanoparticles through the Tollens process. *J Mater Chem*. 2002;12(3):522–527. doi:10.1039/b107469e
51. Mei S, Wang H, Wang W, et al. Antibacterial effects and biocompatibility of titanium surfaces with graded silver incorporation in titania nanotubes. *Biomaterials*. 2014;35(14):4255–4265.
52. Rho JY, Tsui TY, Pharr GM. Elastic properties of human cortical and trabecular lamellar bone measured by nanoindentation. *Biomaterials*. 1997;18(20):1325–1330. doi:10.1016/S0142-9612(97)00073-2
53. Darouiche RO. Treatment of infections associated with surgical implants. *N Engl J Med*. 2004;350(14):1422–1429. doi:10.1056/NEJMra035415
54. Ribeiro M, Monteiro FJ, Ferraz MP. Infection of orthopedic implants with emphasis on bacterial adhesion process and techniques used in studying bacterial-material interactions. *Biomatter*. 2012;2(4):176–194. doi:10.4161/biom.22905
55. Deutscher J, Saier MH Jr. Ser/Thr/Tyr protein phosphorylation in bacteria - for long time neglected, now well established. *J Mol Microbiol Biotechnol*. 2005;9(3–4):656.
56. Shrivastava S, Bera T, Roy A, Singh G, Ramachandrarao P, Dash D. Retracted: characterization of enhanced antibacterial effects of novel silver nanoparticles. *Nanotechnology*. 2007;18(22):225103. doi:10.1088/0957-4484/18/22/225103
57. Cozzone AJ. Role of protein phosphorylation on serine/threonine and tyrosine in the virulence of bacterial pathogens. *J Mol Microbiol Biotechnol*. 2005;9(3–4):56.
58. Morones JR, Elechiguerra JL, Camacho A, et al. The bactericidal effect of silver nanoparticles. *Nanotechnology*. 2005;16(10):2346–2353. doi:10.1088/0957-4484/16/10/059
59. Jung WK, Koo HC, Kim KW, Shin S, Kim SH, Park YH. Antibacterial activity and mechanism of action of the silver ion in Staphylococcus aureus and Escherichia coli. *Appl Environ Microbiol*. 2008;74(7):2171–2178. doi:10.1128/AEM.02001-07
60. Li WR, Xie XB, Shi QS, Zeng HY, Ou-Yang YS, Chen YB. Antibacterial activity and mechanism of silver nanoparticles on Escherichia coli. *Appl Microbiol Biotechnol*. 2010;85(4):1115–1122. doi:10.1007/s00253-009-2159-5
61. Holt KB, Bard AJ. Interaction of silver(I) ions with the respiratory chain of Escherichia coli: an electrochemical and scanning electrochemical microscopy study of the antimicrobial mechanism of micromolar Ag+. *Biochemistry*. 2005;44(39):13214–13223. doi:10.1021/bi0508542
62. Mates JM. Effects of antioxidant enzymes in the molecular control of reactive oxygen species toxicology. *Toxicology*. 2000;153(1–3):83–104. doi:10.1016/S0300-483X(00)00306-1
63. Marambio-Jones C, Hoek EMV. A review of the antibacterial effects of silver nanomaterials and potential implications for human health and the environment. *J Nanopart Res*. 2010;12(5):1531–1551. doi:10.1007/s11051-010-9900-y
64. Dowling DP, Miller IS, Ardhaoui M, Gallagher WM. Effect of surface wettability and topography on the adhesion of osteosarcoma cells on plasma-modified polystyrene. *J Biomater Appl*. 2011;26(3):327–347. doi:10.1177/0885328210372148
65. Wang W, Zhao L, Wu K, et al. The role of integrin-linked kinase/beta-catenin pathway in the enhanced MG63 differentiation by micro/nano-textured topography. *Biomaterials*. 2013;34(3):631–640. doi:10.1016/j.biomaterials.2012.10.021
66. Teisala H, Tuominen M, Kuusipalo J. Adhesion Mechanism of Water Droplets on Hierarchically Rough Superhydrophobic Rose Petal Surface. *J Nanomater*. 2011;2011:1–6. doi:10.1155/2011/818707
67. Stanciu L, Diaz-Amaya S. Chapter 8 - Tissue-biomaterials interactions. In: Stanciu L, Diaz-Amaya S, editors. *Introductory Biomaterials*. Boston: Academic Press; 2022:171–200.
68. Kyriakides TR. Chapter 5 - Molecular Events at Tissue–Biomaterial Interface. In: Badylak SF, editor. *Host Response to Biomaterials*. Oxford: Academic Press; 2015:81–116.

69. Thevenot P, Hu WJ, Tang LP. Surface chemistry influences implant biocompatibility. *Curr Top Med Chem*. 2008;8(4):270–280. doi:10.2174/156802608783790901
70. Wilson CJ, Clegg RE, Leavesley DI, Pearcy MJ. Mediation of biomaterial-cell interactions by adsorbed proteins: a review. *Tissue Eng*. 2005;11(1–2):1–18. doi:10.1089/ten.2005.11.1
71. Silva TMJ, Glee PM, Hazen KC. Influence of Cell-Surface Hydrophobicity on Attachment of Candida-Albicans to Extracellular-Matrix Proteins. *J Med Vet Mycol*. 1995;33(2):117–122. doi:10.1080/02681219580000251
72. Frevert CW, Sannes PL. Matrix proteoglycans as effector molecules for epithelial cell function. *Eur Respir Rev*. 2005;14(97):137–144. doi:10.1183/09059180.05.00009703
73. Frantz C, Stewart KM, Weaver VM. The extracellular matrix at a glance. *J Cell Sci*. 2010;123(24):4195–4200. doi:10.1242/jcs.023820
74. Yang LY, Jiang ZY, Zhou LH, Zhao KL, Ma X, Cheng GS. Hydrophilic cell-derived extracellular matrix as a niche to promote adhesion and differentiation of neural progenitor cells. *Rsc Adv*. 2017;7(72):45587–45594. doi:10.1039/C7RA08273H
75. Rupp F, Scheideler L, Eichler M, Geis-Gerstorfer J. Wetting behavior of dental implants. *Int J Oral Maxillofac Implants*. 2011;26(6):1256–1266.
76. Qin H, Cao HL, Zhao YC, et al. Antimicrobial and Osteogenic Properties of Silver-Ion-Implanted Stainless Steel. *Acs Appl Mater Inter*. 2015;7(20):10785–10794. doi:10.1021/acsami.5b01310
77. Greulich C, Diendorf J, Simon T, Eggeler G, Epple M, Koller M. Uptake and intracellular distribution of silver nanoparticles in human mesenchymal stem cells. *Acta Biomater*. 2011;7(1):347–354. doi:10.1016/j.actbio.2010.08.003
78. Sengstock C, Diendorf J, Epple M, Schildhauer TA, Koller M. Effect of silver nanoparticles on human mesenchymal stem cell differentiation. *Beilstein J Nanotech*. 2014;5:2058–2069. doi:10.3762/bjnano.5.214
79. Nguyen AK, Patel R, Noble JM, et al. Effects of Subcytotoxic Exposure of Silver Nanoparticles on Osteogenic Differentiation of Human Bone Marrow Stem Cells. *Appl in vitro Toxicol*. 2019;5(3):123–133. doi:10.1089/aivt.2019.0001
80. Fu ZY, Hou YL, Haugen HJ, et al. TiO2 nanostructured implant surface-mediated M2c polarization of inflammatory monocyte requiring intact cytoskeleton rearrangement. *J Nanobiotechnol*. 2023;21(1). doi:10.1186/s12951-022-01751-9
81. Koutouzis T, Wallet S, Calderon N, Lundgren T. Bacterial Colonization of the Implant-Abutment Interface Using an In Vitro Dynamic Loading Model. *J Periodontol*. 2011;82(4):613–618. doi:10.1902/jop.2010.100415
82. Tang K, Luo ML, Zhou W, Niu LN, Chen JH, Wang F. The integration of peri-implant soft tissues around zirconia abutments: challenges and strategies. *Bioact Mater*. 2023;27:348–361. doi:10.1016/j.bioactmat.2023.04.009
83. Gulati K, Chopra D, Kocak-Oztug NA, Verron E. Fit and forget: the future of dental implant therapy via nanotechnology. *Adv Drug Deliv Rev*. 2023;199:114900. doi:10.1016/j.addr.2023.114900